

The interaction of charge carriers in superfluid helium with microwave fields—quantum dynamics of a classically chaotic system

E Shimshoni and U Smilansky

Department of Nuclear Physics, The Weizmann Institute of Science, Rehovot 76100, Israel

Received 7 September 1987

Accepted by D K Campbell

Abstract. We compare the classical and quantum descriptions of the response of charge carriers in superfluid helium to an external periodic perturbation. The classical dynamics displays chaotic features, whose main consequence is that the energy gain occurs via a diffusive process. Chaos is limited to the low-energy domain of phase space, and at high excitation energies the dynamics becomes progressively more regular due to the existence of an approximate constant of the motion. The quantum description shows the typical suppression of the classical diffusive energy growth and, at high energies, the quantum analogue of the classical constant of the motion dominates the quantum behaviour.

1. Introduction

Much of our understanding of the quantum dynamics of classically chaotic systems is derived from the study of a few simple examples. The most intensively discussed system is the quantum analogue of the standard map—the quantal *kicked rotor* [1–5]. The quantum mechanical suppression of classical diffusion was discovered here for the first time [1], and in subsequent work [2] it was shown to originate from a localisation mechanism quite analogous to the one responsible for Anderson localisation in a disordered one-dimensional crystal lattice.

The work which followed in this field was aimed at clarifying to what extent the results obtained in the quantum analogue of the kicked rotor apply in the quantum description of other classically chaotic systems. In particular, three main issues were addressed: (a) whether the suppression of classical diffusion is universal, (b) whether the Anderson-like localisation mechanism is common to all quantum systems of this type and (c) what the experimental manifestations of the quantal suppression of classical diffusion are.

The experimental [6–8] and theoretical [9–15] work on the ionisation of Rydberg states in hydrogen atoms was designed to shed light on these questions. There, the

ionisation channel was used to probe the energy transfer to the atom, and to check to what extent the classical diffusion persists in the quantum domain. The answers to the points (a) and (b) above were found to depend on the ratio between the driving field frequency ω and the Keplerian frequency ω_K of the electron in the initial state. For $\omega < \omega_K$, and apart from special cases, both classical and quantum calculations reproduce the experimental ionisation thresholds. A transition between localised and 'delocalised' regimes does occur, but this has nothing to do with the Anderson mechanism. For $\omega > \omega_K$, the theoretical studies suggest a closer similarity to the kicked rotor.

The two examples discussed above are rather different. In table 1 we present a summary of their properties, such as the unperturbed spectra, the structure of the perturbation and its temporal behaviour. With such different characteristics, it is hard to point out the single property that is responsible for the marked difference in the quantum dynamics of the two systems, whose classical description shows similar chaotic features.

The present work was motivated by the need to investigate a system which, in some sense, is intermediate between the kicked rotor and the driven hydrogen atom, and which can be also tested experimentally. We chose to study the response of charge carriers, trapped under the surface of superfluid helium [16-17], to an external microwave field. Each charge carrier consists of a large number (~ 50) of helium atoms, which form a cavity ('bubble') surrounding an electron or an ion. These structures have a very long lifetime and at low temperatures they move as free 'particles' without noticeable dissipation. The 'bubbles' are repelled from the liquid surface by the induced polarisation, and are prevented from escaping into the liquid bulk by a constant electric field F perpendicular to the surface. The resulting potential well is given by

$$V_0 = (A/x) + eFx \quad A = e^2(\epsilon - 1)/4\epsilon(\epsilon + 1) \quad (1.1)$$

where ϵ is the dielectric constant of the liquid. On this bounded system, a sinusoidal microwave perturbation is imposed; since the potential (1.1) is anharmonic, the classical analogue of this system is expected to be chaotic.

Table 1 shows the important features which characterize the 'bubble' system together with those of the kicked rotor and the microwave-driven hydrogen atom. It supports the claim of the former to be 'intermediate' between the latter systems.

Table 1. Comparison of the salient features of the 'bubble' model to other periodically driven systems.

Feature	Kicked rotor	H atom in RF field	'Bubble' in RF field
Unperturbed spectrum (discrete)	$\frac{1}{2}n^2$	$-\frac{1}{2}n^{-2}$	$\frac{3}{2}n^{2/3}$
Unperturbed spectrum (continuum)	—	$\frac{1}{2}k^2$	—
Classical frequency	n	n^{-3}	$n^{-1/3}$
Driving field frequency	$\omega + \text{harmonics}$	ω	$\omega + \text{harmonics}$
Driving field matrix elements:			
diagonal (V_{nn})	0	ϵn^2	$\epsilon n^{2/3}$
off-diagonal (V_{nm})	$\epsilon \delta_{m,n\pm 1}$	$\epsilon n^2 n-m ^{-5/2}$ ($n \gg m$)	$\epsilon n^{-4/3}$ ($n \gg m$)

In the present work we studied a somewhat simplified model for the physical He 'bubbles'. We notice that the essential ingredients in the potential (1.1) are that at short distances it exerts a strong repulsion on the particle, while at large distances the force is attractive and approaches a constant value. This allows a simplification of the 'bubble' problem, where we replace the potential (1.1) by

$$V_0(x) = \begin{cases} eFx & \text{at } x > 0 \\ \infty & \text{at } x = 0. \end{cases} \quad (1.2)$$

To simplify the calculations even further, we replace the pure sinusoidal time dependence of the driving field by a train of δ kicks with alternating signs:

$$V(x, t) = \rho x \sum_{n=-\infty}^{\infty} \delta[t - (2n - 1)\tau] - \delta(t - 2n\tau) \quad (1.3)$$

and

$$H = (p^2/2m) + V_0(x) + V(x, t). \quad (1.4)$$

Thus, both the classical and quantal equations of motion reduce to discrete maps.

Before turning to the solution of this dynamical system we should emphasise a few important points. For a given energy E the unperturbed motion is periodic, with a period $T_0 \sim E^{1/2}$. Thus, as the field pumps more energy to the 'bubble', the ratio between the period T_0 and the field period 2τ increases, and the 'bubble' will experience a large number of field cycles before approaching the potential wall at $x = 0$. Note, however, that in the *absence* of the wall, the Hamiltonian is integrable (being quadratic in the momentum and linear in the coordinate). The system then possesses a constant of the motion

$$G = E + (\rho p/2m) \quad (1.5)$$

which for finite but high energies will dominate the dynamics. The existence of an asymptotic constant of the motion at high energies affects the classical as well as the quantal theory, and is the reason why classical chaos is more pronounced in the low-energy domain of phase space.

We devote the rest of this paper to the study of the classical dynamics (§2) and its quantum analogue (§3). We summarise and discuss our results in §4, and show their relevance to the questions (a)–(c) posed above.

2. Classical dynamics

To write the equations of motion in terms of dimensionless quantities we use an arbitrary energy scale E_s , and the quantities

$$x_0 \equiv E_s/eF \quad p_0 \equiv \sqrt{2mE_s} \quad t_0 \equiv (2E_s m/e^2 F^2)^{1/2}$$

as position, momentum and time scale, respectively. Then, the Hamiltonian in units of E_s is

$$H = \eta^2 + \xi + P\xi\delta_T(t) \quad (2.1)$$

where

$$\xi \equiv x/x_0 \quad \eta \equiv p/p_0 \quad P \equiv \rho/p_0 \quad T \equiv \tau/t_0$$

and

$$\delta_T(t) \equiv \sum_{n=-\infty}^{\infty} \delta[t - (2n - 1)T] - \delta(t - 2nT). \quad (2.2)$$

Between kicks, the motion is periodic, therefore it is natural to work in the action-angle representation (J, ϕ) :

$$J = \frac{2}{3\pi} E^{3/2} \quad \phi = \pi \left(1 - \frac{\eta}{E^{1/2}} \right). \quad (2.3)$$

Here $E^{\lambda} = \eta^2 + \xi$ is the energy, which is constant between kicks. In the following sections, some of the equations are written in terms of a variable χ defined as

$$\chi \equiv \left(\frac{3\pi}{2} J \right)^{1/3} = E^{1/2}. \quad (2.4)$$

χ is easily recognised as half the period of the unperturbed motion:

$$\chi = \pi / (\partial E / \partial J). \quad (2.5)$$

The dynamics of this model can be described by means of an area-preserving mapping of phase space onto itself. Let ϕ_n, J_n be the angle and action, respectively, immediately before the n th positive kick (namely, just before $t = nT$, where n is an odd integer). The mapping $(\phi_n, J_n) \mapsto (\phi_{n+1}, J_{n+1})$ is constructed in three steps.

1. Denote by the subscript $n+$ each variable immediately after the positive kick. Then:

$$\eta_{n+} = \eta_n + P \quad \xi_{n+} = \xi_n \quad E_{n+} = E_n + 2\eta_n P + P^2.$$

Hence

$$\chi_{n+} = (\chi_n^2 + 2P\chi_n(1 - \phi_n/\pi) + P^2)^{1/2} \quad \phi_{n+} = \pi \left(1 - \frac{\eta_{n+}}{E_{n+}^{1/2}} \right). \quad (2.6)$$

2. After a time interval T , just before the next (negative) kick:

$$\bar{J}_n = J_{n+} \quad \bar{\phi}_n = \left(\phi_{n+} + \frac{\partial E_{n+}}{\partial J_{n+}} T \right) \bmod 2\pi$$

and one obtains for the intermediate $\bar{\chi}_n$ and $\bar{\phi}_n$

$$\bar{\chi}_n = \chi_{n+} \quad \bar{\phi}_n = \pi \left(1 + \frac{T - P}{\bar{\chi}_n} + \frac{\chi_n(\phi_n/\pi - 1)}{\bar{\chi}_n} \right) - 2\pi K_n \quad (2.7)$$

where

$$K_n \equiv \left[\frac{\bar{\chi}_n + T - P + \chi_n(\phi_n/\pi - 1)}{2\bar{\chi}_n} \right]$$

(the square brackets denote the integer value). K_n counts the number of collisions with the wall between a positive and a negative kick (namely, within the first half of the field cycle.)

3. Immediately after the negative kick, steps 1 and 2 repeat in the same way (where P is replaced by $-P$, and the initial conditions are $\bar{\chi}_n, \bar{\phi}_n$ instead of χ_n, ϕ_n).

The result is the desired mapping:

$$\begin{aligned} \chi_{n+1} &= (\chi_n^2 + 2P(T - 2\tilde{\chi}_n K_n))^{1/2} \\ \phi_{n+1} &= \pi \left(1 + \frac{2T + \chi_n(\phi_n/\pi - 1) - 2K_n \tilde{\chi}_n}{\chi_{n+1}} \right) - 2\pi \tilde{K}_n \end{aligned} \quad (2.8)$$

where

$$\tilde{K}_n \equiv \left[\frac{\chi_{n+1} + 2T + \chi_n(\phi_n/\pi - 1) - 2K_n \tilde{\chi}_n}{2\chi_{n+1}} \right].$$

\tilde{K}_n is the number of collisions with the wall within the second half of the field cycle.

The mapping (2.8) is very complicated and hence hard to interpret analytically. However, the dependence of the integers K_n and \tilde{K}_n upon the action variable can shed some light on the behaviour of the system in the extreme domains of phase space. At low energies, χ is small and hence, within a field cycle, the particle hits the wall several times ($\tilde{K}_n, K_n > 1$); in this domain classical chaos is expected. At high energies χ is large, and once it exceeds T appreciably ($\tilde{K}_n, K_n = 0$), the motion becomes more regular. From (2.8) one can see that, as long as $K_n = 0$, the energy (χ_n^2) at each n increases by a constant amount ($2PT$); the quantity G defined in (1.5) is then a constant of the map throughout a large number of iterations. This general behaviour is demonstrated in figure 1, where a trajectory is traced in phase space. The transition between the strongly chaotic domain at low energies and the almost regular motion at high energies is apparent.

One can also learn about the dynamics of the system through the stability properties of its fixed points, for which

$$(\chi_{n+1}, \phi_{n+1}) = (\chi_n, \phi_n) \equiv (\chi^*, \phi^*).$$

The resulting fixed points are

$$\chi^* = \frac{T}{2\tilde{K}^*} \quad \phi^* = \pi \left\{ 1 - \frac{\tilde{K}^*}{PT} \left(\frac{T^2}{4} \left(\frac{1}{(K^*)^2} - \frac{1}{(\tilde{K}^*)^2} \right) - P^2 \right) \right\}. \quad (2.9)$$

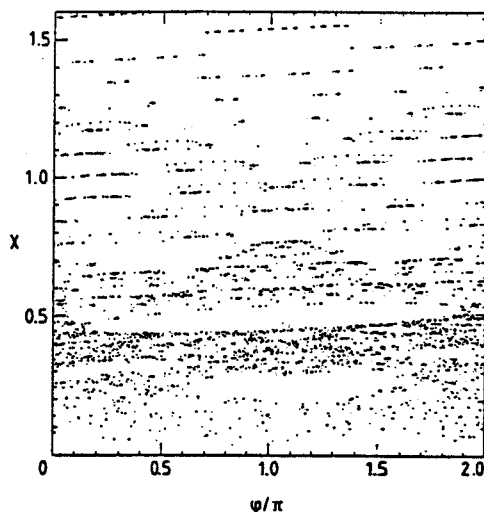


Figure 1. A typical classical trajectory ($P = 0.08$, $T = 1.0$).

The positive integers K^* and \tilde{K}^* were defined in (2.7) and (2.8), respectively. No fixed point exists for $\tilde{K}_n = 0$. In view of the physical meaning of the above integers, the fixed-point condition on the action variable can be easily understood: all the χ^* correspond to resonances, which occur when the period of the perturbation and the unperturbed period are rationally related to each other. Nevertheless, as will be shown below, not all the resonances correspond to fixed points, and this is a peculiar and unique feature of this problem.

By analogy with other studies of chaotic classical systems, our central aim is to characterise the conditions in which one observes *global chaos*. In order to estimate the stochastic parameter in which a transition to global chaos occurs, we use Chirikov's resonance overlap criterion [18]. Writing the interaction as a double Fourier expansion in t and ϕ , one can easily see that resonances occur for the set of J_r :

$$J_r = \frac{2}{3\pi} \left(\frac{Tm}{k} \right)^3 \quad \text{for } m, k \text{ integers} \quad (2.10)$$

i.e. when the unperturbed period is a rational multiple of the period of kicks:

$$\chi_r = \frac{m}{k} T.$$

Using standard methods, we calculated for each resonance J_r the separatrix half-width in the (J, ϕ) phase space:

$$\Delta J_r = \frac{6\sqrt{4P/T} J_r}{m\pi}. \quad (2.11)$$

From (2.11) it is clear that as the stochastic parameter P/T grows, the width is getting bigger, while the distance separating two successive resonances does not depend on P/T . For each resonance there exists a critical value of P/T for which it overlaps with its nearest neighbour, and vice versa—for each P/T there is a critical J up to which all adjacent resonances overlap. The criterion for overlapping of two resonances which are a distance ΔJ apart is simply

$$\frac{2\Delta J_r}{\Delta J} \geq 1. \quad (2.12)$$

Inserting the resonance condition (2.10) for $k \gg 1$ and $m = 1$, the relation between the critical P/T and J becomes

$$J_{cr}(P, T) = \frac{2}{3\pi} (4P/T)^{3/2} \left(\frac{4T}{\pi} \right)^3 = \frac{4}{3} \left(\frac{4}{\pi} \right)^4 (PT)^{3/2}. \quad (2.13)$$

As for the high- m and low- k resonances, they are embedded in the region where regular trajectories dominate the dynamics (for low T/χ values). These structures are not of the generic type for which the Chirikov criterion is designed.

In most of the classical chaos problems, the above results would be enough to understand how different types of trajectories in phase space behave: for small stochastic parameters, at each J_r there exists an even number of fixed points (or cycles of some order), stable and unstable alternatively. Trajectories starting near the stable cycle would be regular closed orbits, forming an island chain. Those starting near the unstable fixed points would form a thin stochastic layer. In the

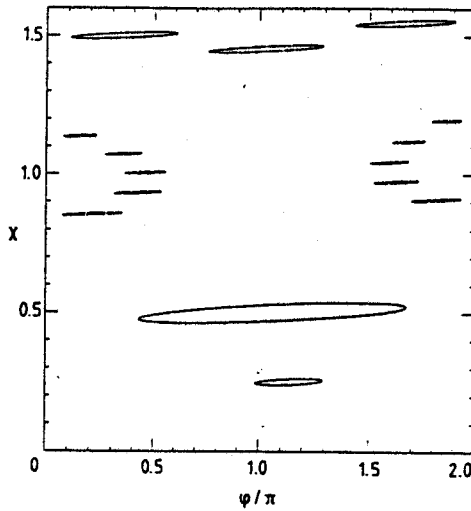


Figure 2. A classical trajectory near the resonances $\chi = \frac{3}{2}$, 1, $\frac{1}{2}$ and $\frac{1}{4}$ ($P = 0.08$, $T = 1.0$).

present problem the behaviour is somewhat different: concentrating upon primary resonances ($m = 1$), we see that the resonances $\chi_r = T/k$ with *odd* k do not correspond to fixed points of the mapping as determined by (2.9). The iteration of the mapping in the vicinity of such resonances indeed reveals uncommon features: the trajectories form series of stripes (see figure 2 in the vicinity of $\chi = 1$ and figure 3). This is in contrast with the generic behaviour of trajectories near resonances with even k values (figure 2 near $\chi = \frac{1}{4}$, $\frac{1}{2}$ and $\frac{3}{2}$).

To understand the origin of the non-generic trajectories, consider the mapping (2.8) in the limit $P/\chi \rightarrow 0$. Denote by $\delta\chi$ the difference $\chi_{n+1} - \chi_n$; then to first order

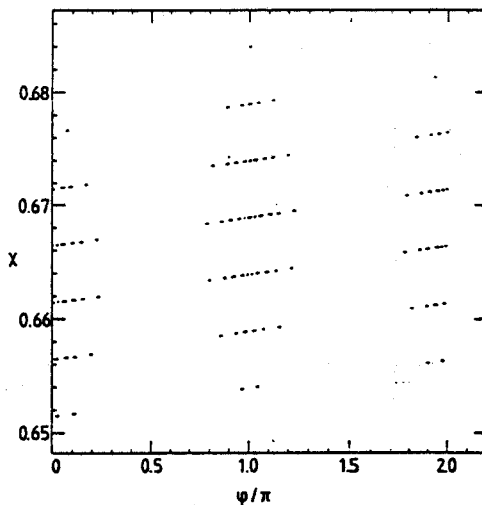


Figure 3. A classical trajectory near a non-generic resonance: $\chi = \frac{2}{3}$, $P = 0.005$, $T = 1.0$.

in P/χ

$$\delta\chi \approx \frac{P}{\chi_r} (T - 2K_n \chi_r) = P \left(\frac{k}{m} - 2K_n \right) \quad (2.14)$$

where χ_r is the average value of χ_n which satisfies the *exact* resonance condition (i.e. $\chi_r/T = m/k$), and k is the value of K_n when χ_n coincides with χ_r . In the same manner, we define the change in phase $\delta\phi \equiv \phi_{n+1} - \phi_n$. Then, to zeroth order in P/χ

$$\delta\phi \approx \frac{2\pi T}{\chi_r} = \frac{2\pi k}{m}. \quad (2.15)$$

If the conditions for the above approximation to hold are satisfied, the motion in the (ϕ, J) phase space is such that in the vicinity of J_r the action grows almost linearly with the angle (like a regular wrapping of a thread around a cylinder). Changing variables from χ to J , one obtains the slope of the linear growth in the (ϕ, J) plane:

$$\frac{\delta J}{\delta\phi} = \frac{3}{2\pi} P ((2/3\pi)^{1/3} J_r^{2/3} T - 2k J_r). \quad (2.16)$$

The slope was computed numerically in several cases from the trajectory, and agreed with (2.16) within an error of 5–10%.

The ‘thread wrapping’ motion described here continues up to a certain point, where a jump to a lower action occurs, still within the same set of stripes. The jumps happen when K_n changes, and this introduces a discontinuity since K_n is defined as an integer value (2.7). We estimate the point in phase space at which K_n changes, by considering the expression inside the integer value. Thus, near each resonance corresponding to χ_r , a ‘jump’ occurs whenever ϕ_n exceeds ϕ_c , where

$$\phi_c \approx \pi \left(2k - \frac{T}{\chi_r} \right). \quad (2.17)$$

This was also checked to agree with the numerical results.

The above discussion is valid only as long as the first-order contribution to $\delta\chi$ does not vanish; otherwise, $\delta\chi$ is dominated by higher orders in P/χ , which are much more complicated. The right-hand side of (2.14) indeed vanishes if $\chi = T/2k$ —i.e. near a fixed point of the mapping. Hence, the behaviour of trajectories in the vicinity of even- k resonances does not form a series of stripes as described above. Rather, structures similar to the standard island chains dominate the dynamics.

The appearance of non-generic trajectories in this problem is, in fact, a consequence of the non-analyticity of the mapping. Due to the discontinuity of the momentum near the wall, a stable fixed point cannot exist in the vicinity of the wall (i.e. near $\phi = 0$ or $\phi = 2\pi$). Hence, the generic structures are preserved only in the vicinity of fixed points (or higher-order cycles), which are far enough from the wall.

For several J_r values we calculated numerically the width ΔJ_r of the area in phase space, which is occupied by a near-resonance trajectory; it was in good agreement with the width (2.11) predicted by the resonance overlap theory, for the generic as well as for the ‘non-conventional’ resonances.

From the above discussion a general description of phase space was constructed,

and it is pictorially represented by figures 1 and 2. For values of P , T which are small compared with χ , there are two types of bounded trajectories: near fixed point (at even- k resonances) and series of stripes (near odd- k resonances). One can expect a chaotic behaviour only at low energies, such that χ is smaller than

$$\chi_u \sim T. \quad (2.18)$$

Above χ_u the motion is more regular (this domain will be discussed separately at the end of this section). A more quantitative way to demonstrate the reduction of stochasticity at high energies is by calculating the local Lyapunov exponent, or the trace of the linearised map. For small P/χ_n , the approximated trace is

$$\frac{\partial J_{n+1}}{\partial J_n} + \frac{\partial \phi_{n+1}}{\partial \phi_n} \approx 2 + \frac{P}{\chi_n} \left(\frac{3T}{\chi_n} + 2d_n - 4K_n \right) \quad (2.19)$$

where

$$d_n \equiv \frac{T + P((\phi_n/\pi)^2 - 2\phi_n/\pi)}{2\tilde{\chi}_n}.$$

For high χ_n the trace is slightly greater than 2 and therefore the motion is unstable, but it falls to the marginal value 2 as $\sim 1/\chi_n^2$.

Below χ_u , the primary ($m = 1$) fixed-point-type resonances become dense at low actions. Except for islands of stability around the fixed points themselves, the motion in this neighbourhood is strongly unstable. For every rational value of T/χ , series of stripes exist among generic resonances, which are also unstable at low energies. At marginal energies ($\chi \sim \chi_u$), there are bounded trajectories near primary resonances only for $P \ll \chi$; when P is increased, higher order ($m \gg 1$) resonances become important and interfere with the primary structures. The overlap criterion (2.13) cannot be precisely tested, since numerically it is impossible to define a sharp critical stochastic parameter for global chaos at a given initial condition. Even at low perturbations there are no clear separatrices and thin layers, as assumed by the resonance overlap theory, and hence the criterion (2.13) should be modified. A more exact criterion should take into account that the unstable trajectories always merge into a neighbouring series of stripes. However, the upper limit on the energy under which global chaos exists is, indeed, an increasing function of the product PT .

The only remaining task is to find a good measure of chaoticity for the present system. Asymptotic quantities such as the Lyapunov exponent, or the diffusion coefficient defined below—are practically meaningless here, since the instability varies strongly with the energy (or action): most of the unstable trajectories wander over a wide range of actions, and finally escape to the almost regular high-energy regime. However, the rate of energy diffusion turns out to be a useful measure of global chaos in this system. Assume that in a certain regime in phase space the motion is approximately random; we choose an ensemble of trajectories in this regime, all starting with the same energy E_0 . After a time interval NT ($N/2$ iterations of the map), the average over the ensemble of the final energy moments $\langle E_N \rangle$, $\langle E_N^2 \rangle$ can be found numerically. Instead of the asymptotic diffusion coefficient, defined as

$$D \equiv \lim_{N \rightarrow \infty} \frac{\langle \Delta E_N^2 \rangle}{N} \quad \text{where} \quad \langle \Delta E_N^2 \rangle \equiv \langle E_N^2 \rangle - \langle E_N \rangle^2$$

we used the N -dependent quantity

$$D_N \equiv \frac{\Delta E_N^2}{N}. \quad (2.20)$$

If the randomness assumption is true, one expects a linear drift of the average energy:

$$\langle E_N \rangle = E_0 + NP^2. \quad (2.21)$$

Similarly, assuming also that on average there are no correlations between velocities at different times, and also that

$$\langle E_i(1 - \phi_i)^2 \rangle = \langle E_i \rangle \langle (1 - \phi_i)^2 \rangle$$

the N -dependent diffusion rate becomes

$$D_N = \frac{2}{3}(2P^2E_0 + P^4) + \frac{2}{3}P^4(N + 1). \quad (2.22)$$

Hence, under the above assumptions we expect the numerical D_N to grow linearly in time, similarly to the average energy.

Numerical computations of the diffusion of energy as a function of time show that diffusion persists as long as $\chi < T$. In some cases it was indeed approximately growing linearly as a function of N . In order to check how much these results agree with the theory, we computed as a function of $\langle E_N \rangle$ the following ratio:

$$R(N) \equiv \frac{3D_N}{2P^2\langle E_N \rangle}. \quad (2.23)$$

If $N \gg 1$ and $NP^2 \gg E_0$, and if the above assumptions were exact, $R(N)$ should be constant as a function of N , and equal to 1. In figure 4, some typical results of the computation are shown together with their associated phase-space picture. After exploring many graphs of this kind for different P and T , we found a regime in the parameter space (P, T) for which (2.23) was constant within $\pm 20\%$. The value of this constant is shown in figure 5 as a function of P for several T . All the numerical computations used for figure 4 were done with the same initial energy $E_0 = 10^{-4}$, an ensemble of 50 trajectories, and $N \leq 100$. From (2.21) one can calculate the N for which the trajectories are guaranteed to stay below χ_u . Indeed, the reason for the deviations at $T = 1$ and $P > 0.1$ (figure 5) is that the trajectories enter the regime $\chi > \chi_u$. As for the other deviations in figure 5, at lower P , they are due to stable islands whose measure in phase space is significant so that the uniform angle assumption is violated. Figure 5 also shows, that for the same P , E_0 the agreement with the diffusion theory usually improves for greater T ; this is simply because enlarging T is equivalent to lowering the energy at constant T , and thus demonstrating the suppression of stochasticity at high energies.

At the high-energy domain ($\chi \gg T$), many cycles of the field are completed between two adjacent collisions with the wall. Within this time interval the motion is regular and the quantity G (equation (1.5)) is constant. However, once every χ/T iterations of the map the particle hits the wall. Then, the value of G may either change or stay unchanged, depending on the sign of the momentum transfer which follows the collision with the wall. This sign is random if the initial phase of the trajectory is randomly chosen; hence, one expects a diffusive behaviour of the

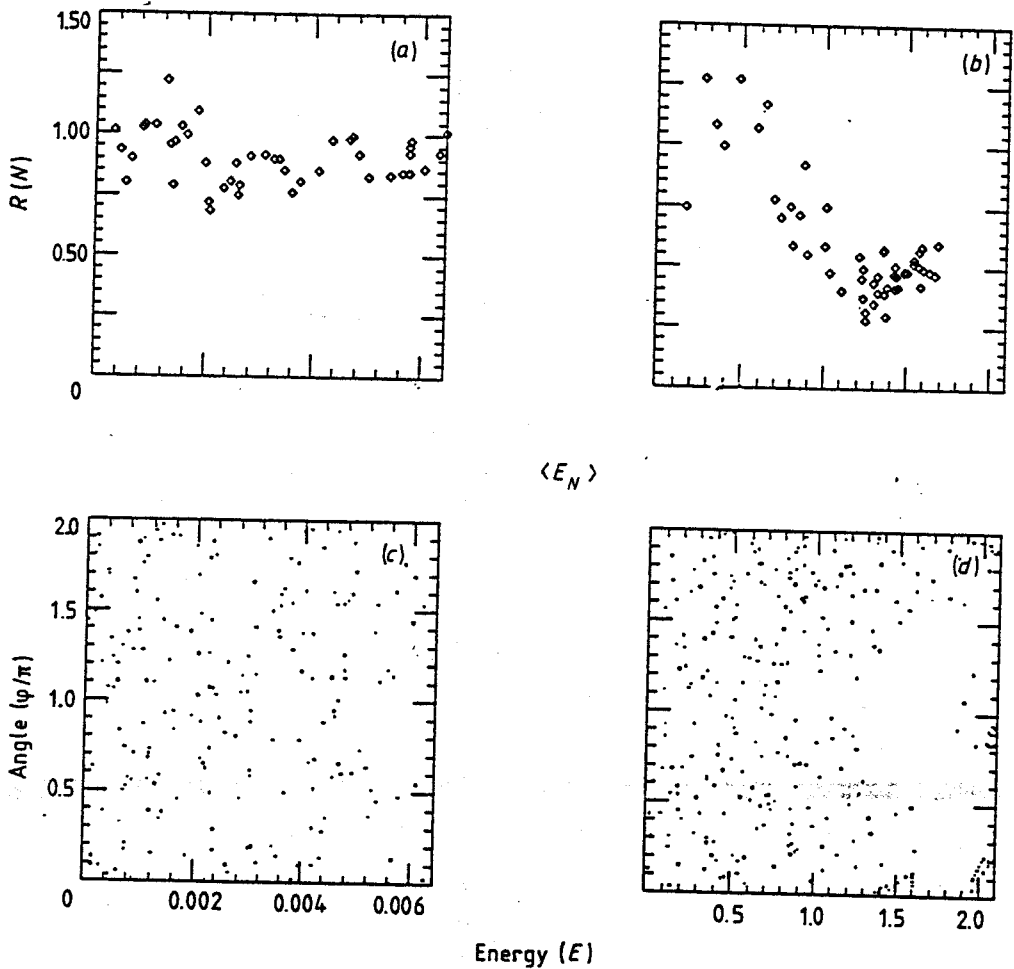


Figure 4. Check of the validity of the simple model for the diffusion (equation (2.23)); (a), (b) the ratio $R(N) = 3D_N/2P^2\langle E_N \rangle$ as a function of $\langle E_N \rangle$; (c), (d) a typical trajectory in the corresponding ensemble; (a), (c) $P = 0.008$, $T = 20.0$; (b), (d) $P = 0.2$, $T = 10.0$. Note that deviations from $R(N) = 1$ coincide in energy with the occurrence of a stable island in phase space.

motion, whose rate is χ/T times slower than the rate of diffusion in the chaotic regime.

In order to demonstrate the main difference between the high- and low-energy domains, we repeated the calculations of $\langle E_N \rangle$ and D_N in the limit where E_0 is very high (compared with both P^2 and T^2). Consider first a single trajectory in the ensemble. Between two collisions with the wall, the increase in χ at each iteration of the map is given by (2.14) with $K_n = 0$. Hence, the total increase in χ just before the next collision with the wall is P . Denote by χ_i the value of χ just after the i th collision; then

$$\chi_{i+1} = \begin{cases} \chi_i + P & K_{i+1} = 0 \\ \chi_i - P & K_{i+1} = 1 \end{cases} \quad (2.24)$$

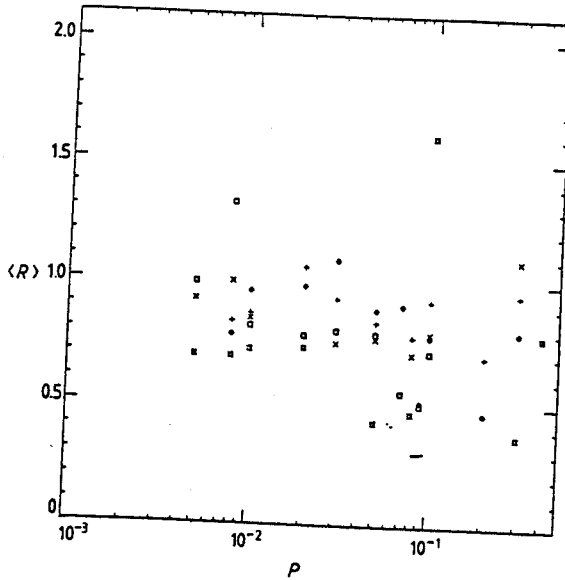


Figure 5. The N -averaged value $\langle R \rangle = (1/N) \sum R(N)$ as a function of P for various T values: +, $T = 50$; \times , $T = 20$; \diamond , $T = 10$; \square , $T = 5$; $*$, $T = 1$.

$K_{i+1} = 0$ if G is not changed by the collision. Assuming an ensemble of such trajectories, in which the probability for G to change or not to change is equal, then one obtains

$$\langle E_N \rangle = \langle \chi_N^2 \rangle = E_0 + \frac{T}{E_0^{1/2}} NP^2 \quad \text{and} \quad D_N = 4TP^2 E_0^{1/2} + \frac{T^2}{E_0} NP^4. \quad (2.25)$$

These predictions were confirmed by numerical calculations for various parameters and initial energies in the 'far-wall' limit.

Comparing (2.25) with the corresponding quantities in the chaotic regime (2.21) and (2.22), one can point out that the expressions are similar, apart from one major difference: at high energies, both the drift of the average energy and D_N are smaller than the low-energy quantities by a factor of $\sim E_0^{1/2}/T$. That is, for fixed P and T the rate of diffusion is indeed reduced as the energy grows. In addition, if one considers the drift of $\langle E_N \rangle$ relative to the initial value E_0 , within our approximation it is smaller with respect to the relative drift at low energies also because $P^2 \ll E_0$.

To summarise: the classical description of the 'bubble' indicates the existence of chaotic domains in phase space; the chaotic behaviour gives rise to a fast diffusion of energy. Among the typical structures in phase space one can identify generic as well as non-generic structures; the latter are special for this particular model. In the low-energy domain, the two types of structure are intricately interwoven, hence introducing strong stochasticity; above some critical energy, the collisions with the wall become rare, and hence the chaotic features are suppressed. In general, the stochasticity decreases as a function of the energy, and at high energies it approaches the 'far-wall' limit, in which the motion is almost regular.

3. The quantum dynamics

In this section we discuss the quantum mechanical description of the model introduced in §2. The unperturbed system is characterised by the quantum analogue of H_0 (2.1). The corresponding Schrödinger equation is

$$\left(-\frac{\hbar^2}{2m} \frac{d^2}{dx^2} + eFx\right)\psi(x) = E\psi(x) \quad (3.1)$$

together with boundary conditions on the wavefunctions

$$\psi(0) = 0 \quad \text{and} \quad \lim_{x \rightarrow \infty} \psi(x) = 0.$$

The boundary condition at $x=0$ is the quantum analogue of the classical perfect reflection from the wall. We rewrite (3.1) in terms of the dimensionless coordinate and energy, defined as

$$z \equiv \alpha eFx \quad \varepsilon \equiv \alpha E \quad \text{where} \quad \alpha \equiv \left(\frac{2m}{\hbar^2(eF)^2}\right)^{1/3}. \quad (3.2)$$

For each ε , the corresponding Schrödinger equation becomes

$$-\frac{\partial^2 \psi}{\partial y^2} + y\psi = 0 \quad \text{where} \quad y \equiv z - \varepsilon. \quad (3.3)$$

The solution for (3.3), together with the boundary conditions is the set of functions

$$\langle z | j \rangle \equiv \psi_j(z) = \begin{cases} C_j \text{Ai}(z - \varepsilon_j) & z \geq 0 \\ 0 & z < 0 \end{cases} \quad C_j \equiv \frac{(2eF)^{1/2}}{\text{Ai}'(-\varepsilon_j)}. \quad (3.4)$$

$\text{Ai}(x)$ is Airy's function, $(-\varepsilon_j)$ are the zeros of $\text{Ai}(x)$ [19]:

$$\varepsilon_j = f\left(\frac{3\pi}{8}(4j-1)\right) \quad j \text{ integer}$$

and

$$f(\xi) \equiv \xi^{2/3} \left(1 + \frac{5}{48} \frac{1}{\xi^2} - \frac{5}{36} \frac{1}{\xi^4} + \dots\right) \quad \text{for } \xi \gg 1. \quad (3.5)$$

The quantum number j is the quantum analogue of the classical action; in the semiclassical limit, (3.5) recovers the classical relation between energy and action (2.3) and $\varepsilon_j \sim j^{2/3}$. This behaviour of the spectrum is one of the special characteristics of the quantum 'bubble', since it implies that the separation between energy levels is converging ($\Delta\varepsilon \sim 1/j^{1/3}$). In addition, this system is bounded; therefore, the energy spectrum is discrete, and the states (3.5) form a complete basis for the allowed physical states.

On the stationary system described above, a time-dependent perturbation is imposed. Since the perturbation $V(z, t)$ is a periodic series of δ kicks, the quantum dynamics may be expressed by means of a *quantum map*. Denote by $|\psi_n\rangle$ the state

of the system just before the n th positive kick; then

$$|\psi_{n+1}\rangle = U(\mathcal{T}, \mathcal{P}) |\psi_n\rangle$$

where

$$\mathcal{T} \equiv \frac{\tau}{\alpha \hbar} \quad \mathcal{P} \equiv \frac{\rho}{e F \alpha \hbar}$$

and

$$U(\mathcal{T}, \mathcal{P}) = \exp(-i\mathcal{T}\hat{\epsilon}) \exp(i\mathcal{P}\hat{z}) \exp(-i\mathcal{T}\hat{\epsilon}) \exp(-i\mathcal{P}\hat{z}). \quad (3.9)$$

($\hat{\epsilon}$ and \hat{z} are the dimensionless unperturbed Hamiltonian and position operators, respectively.) The quantum mechanical dimensionless parameters \mathcal{P} and \mathcal{T} can be related to the dimensionless classical parameters P and T in terms of the quantum energy ϵ_j :

$$P = \frac{\mathcal{P}}{\epsilon_j^{1/2}} \quad T = \frac{\mathcal{T}}{\epsilon_j^{1/2}}. \quad (3.10)$$

$\epsilon_j = (\frac{3}{2}\pi j_s)^{2/3}$ where the quantum number j_s is related to the classical energy scale E_s through $j_s = (2/3\pi\hbar)E_s^{3/2}$. Thus, for a given E_s ,

$$\mathcal{P} \sim \frac{P}{\hbar^{1/3}} \quad \mathcal{T} \sim \frac{T}{\hbar^{1/3}}. \quad (3.11)$$

The propagator $U(\mathcal{T}, \mathcal{P})$ can be expressed as

$$U(\mathcal{T}, \mathcal{P}) \equiv \exp(-i2\hat{W}\mathcal{T}) \quad (3.12)$$

where the Hermitian operator \hat{W} is the quasi-energy (QE) operator [20, 21]. Denote by $|\lambda\rangle$ and ω_λ the QE eigenvectors and eigenvalues, respectively; then, the initial state $|\psi_0\rangle$ develops after N iterations of the quantum map to the state

$$|\psi_N\rangle = \sum_\lambda \exp(-i\omega_\lambda 2N\mathcal{T}) \langle \lambda | \psi_0 \rangle |\lambda\rangle. \quad (3.13)$$

It is convenient to present the propagator as a matrix in the $|j\rangle$ basis, in which it is diagonal with eigenvalues ϵ_j . In this representation

$$\langle j | U(\mathcal{T}, \mathcal{P}) | k \rangle = \sum_l \langle j | \exp(-i\mathcal{T}W_+) | l \rangle \langle l | \exp(-i\mathcal{T}W_-) | k \rangle$$

where

$$\langle j | \exp(-i\mathcal{T}W_\pm) | l \rangle \equiv \exp(-i\mathcal{T}\epsilon_j) \langle j | \exp(\pm i\mathcal{P}\hat{z}) | l \rangle. \quad (3.14)$$

Hence, the calculations reduce to the evaluation of the matrix elements of the kick propagator:

$$I_{jk}(\mathcal{P}) \equiv \langle j | \exp(i\mathcal{P}\hat{z}) | k \rangle. \quad (3.15)$$

The matrix elements of the position operator can be calculated analytically [22]:

$$\langle j | \hat{z} | k \rangle = \begin{cases} \frac{-2}{(\epsilon_j - \epsilon_k)^2} & \text{if } j \neq k \\ \frac{2}{3}\epsilon_j & \text{if } j = k. \end{cases} \quad (3.16)$$

However, it is impractical to calculate the propagator by diagonalising (3.14) in a truncated basis, because of the very slow convergence of the \hat{z} eigenstates with the basis size. Instead, we developed a method to calculate $I_{jk}(\mathcal{P})$ directly. This method, which allows us to obtain $I_{jk}(\mathcal{P})$ to any desired accuracy, is described in the appendix.

An example of the resulting matrix is presented in figure 6: for any row j , the absolute value of $I_{jk}(\mathcal{P})$ is a smooth function of k . As j grows, the diagonal elements decrease and the first near-diagonals become dominant. For $k \gg j$, $I_{jk}(\mathcal{P})$ decreases as a power law in $|k - j|$. The power was estimated numerically to be approximately $-\frac{4}{3}$ (see the appendix).

To study the high- j behaviour of the OE spectrum, we make use of the fact that at

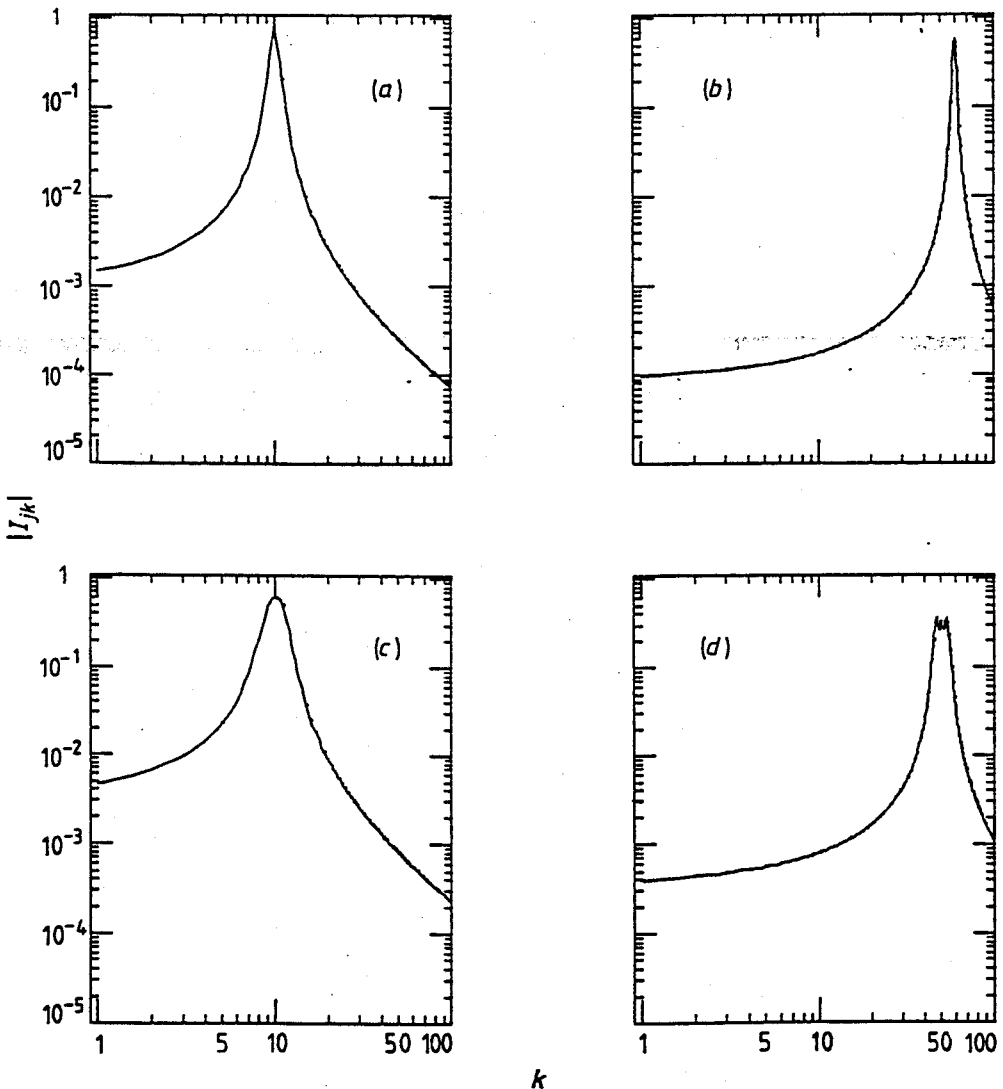


Figure 6. Matrix elements of the 'lock' propagator (equation (3.13)): (a) $\mathcal{P} = 0.08$; $j = 10$; (b) $\mathcal{P} = 0.08$, $j = 60$; (c) $\mathcal{P} = 0.25$, $j = 10$; (d) $\mathcal{P} = 0.25$, $j = 50$.

high excitation energies, many cycles of the field are completed before the 'bubble' is reflected from the wall. We expect therefore that the QE operator in this limit can be approximated by the one calculated by neglecting the presence of the wall altogether. Using simple algebra and the Hausdorff-Baker expansion [23], it is easily shown that the QE in the absence of the wall is

$$\hat{W} = \hat{\varepsilon} + \mathcal{P}\hat{p} \quad (3.15)$$

which is the quantum analogue of the asymptotic classical constant of the motion (1.5).

Reintroducing the wall (i.e. imposing the boundary conditions (3.2)), we have to define the operators $\hat{\varepsilon}$, \hat{p} and \hat{z} in terms of their matrix elements in the $|j\rangle$ representation. Thus

$$\begin{aligned} \langle j | \hat{p} | k \rangle &= \frac{i}{2} \langle j | [\hat{\varepsilon}, \hat{z}] | k \rangle \\ &= (\delta_{jk} - 1) \frac{i}{(\varepsilon_j - \varepsilon_k)} = -i \int_0^\infty \psi_j(z) \frac{\partial}{\partial z} \psi_k(z) dz. \end{aligned} \quad (3.16)$$

However

$$\langle j | [\hat{p}, \hat{z}] | k \rangle = -i \left[(1 - \delta_{jk}) \left(\frac{2}{3} + \sum_{l \neq j, k} \frac{2(\varepsilon_j + \varepsilon_k - 2\varepsilon_l)}{(\varepsilon_j - \varepsilon_l)^2 (\varepsilon_k - \varepsilon_l)^2} \right) + \delta_{jk} \sum_{l \neq j} \frac{4}{(\varepsilon_j - \varepsilon_l)^3} \right]. \quad (3.17)$$

This implies that the Hausdorff-Baker expansion for the evolution operator (3.12) does not close, and that (3.15) cannot be an exact result. The deviation $\Delta(j, k)$ of $\langle j | [\hat{p}, \hat{z}] | k \rangle$ from the canonical expression may indicate the range of validity of the 'far-wall' expression. We see in figure 7 that the deviations in the commutator matrix elements increase as $|j - k|$ increases but, for low differences, the deviations are rather small; for large j but fixed $|j - k|$, they are almost independent of j .

We examined the quantum evolution in two regimes—the classically chaotic regime ($\mathcal{T}/j^{1/3} \gg 2\pi$) and the 'far-wall' regime where the classical diffusion is

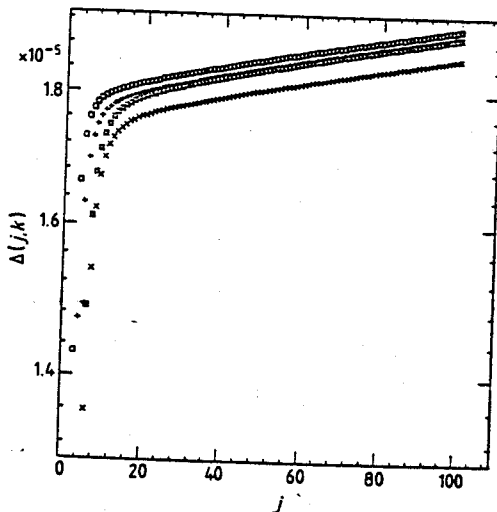


Figure 7. Deviation of $[\hat{p}, \hat{z}]$ from a constant: $\Delta(j, k) = |\langle j | [\hat{p}, \hat{z}] | k \rangle - \delta_{jk}|$; \times , $k = j$; $+$, $k = j + 10$; \square , $k = j + 30$.

suppressed due to the existence of an asymptotic constant of the motion ($\mathcal{F}/j^{1/3} \ll 2\pi$).

The QE spectrum and eigenstates were obtained by diagonalising numerically the propagator (3.12). Special care was taken (see the appendix) to preserve the unitarity of the operator in the truncated space, and to ensure that the conclusions are not affected by the finite basis size. Typical QE eigenstates in the $|j\rangle$ representation are shown in figure 8.

In the classically chaotic regime (figure 8(a) and (b)), the eigenstates are localised over a few j states. The expansion amplitudes fall off rather quickly, and this decrease is modulated by large fluctuations. The fluctuations at low \mathcal{P} values reflect the possibility of resonant transitions between states which satisfy

$$\mathcal{F} |j^{2/3} - k^{2/3}| \left(\frac{32\pi}{9}\right)^{-1/3} = n \quad n \text{ integer} \quad (3.18)$$

(see figure 8(d)). At higher \mathcal{P} values one cannot assign the structures to a simple

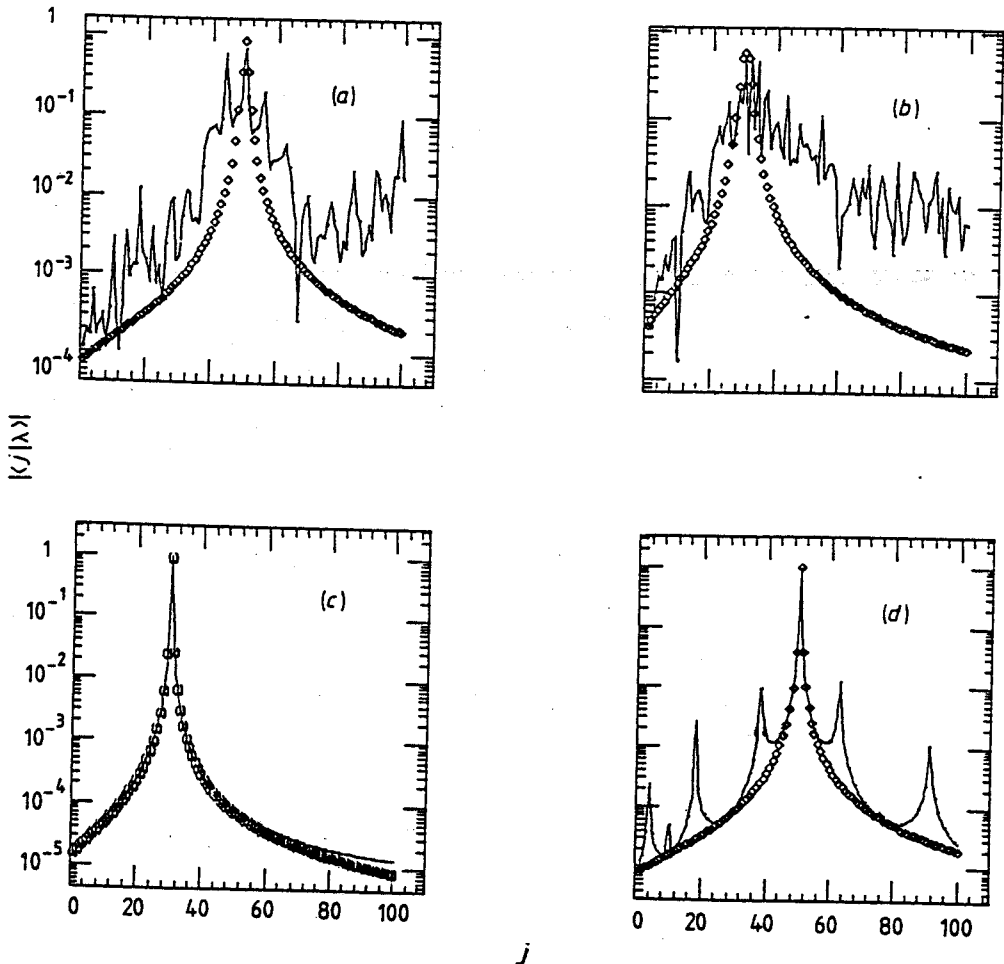


Figure 8. QE eigenstates: (a) $\mathcal{P}=0.1$, $\mathcal{F}=1.0$, $\lambda=50$; (b) $\mathcal{P}=0.25$, $\mathcal{F}=250$, $\lambda=30$; (c) $\mathcal{P}=0.01$, $\mathcal{F}=0.05$, $\lambda=30$; (d) $\mathcal{P}=0.01$, $\mathcal{F}=0.5$, $\lambda=50$. \diamond denotes 'far wall'.

resonance mechanism. On average, the rapid fall of the expansion amplitudes is levelled off at large distances, where a power-law decrease of the QE eigenstates takes over. The reason for this behaviour will be discussed later in this section.

In spite of the fact that the QE eigenstates do not show an exponential localisation throughout the entire j domain, the initial fall-off near the localisation centre may be fitted on the average by an exponential, and a mean localisation length can be extracted. We limited our attention to QE states whose localisation centres are in the range $40 \leq j \leq 60$, so that the effects of the truncated basis will be small. Within this range, and for any given \mathcal{P} and \mathcal{T} values, the localisation length is almost constant. In figure 9 we show the mean localisation length $L(\mathcal{P})$ as a function of \mathcal{P} , for a few \mathcal{T} values in the classically chaotic regime. For a given \mathcal{P} value, $L(\mathcal{P})$ is independent of \mathcal{T} (similarly to the classical diffusion rate). For a fixed value of \mathcal{P} , $L(\mathcal{P})$ increases monotonically with \mathcal{P} , but the dependence on \mathcal{P} is closer to linear rather than to quadratic. This behaviour is inconsistent with the expectation that the localisation length is proportional to the classical diffusion constant.

For small \mathcal{P} and \mathcal{T} , the states are very similar to the eigenstates of the 'far-wall' quasi-energy, denoted by $|\lambda^{(fw)}\rangle$ (diamond symbols in figure 8). These states satisfy the equation

$$\hat{W} |\lambda^{(fw)}\rangle = \omega_{\lambda^{(fw)}} |\lambda^{(fw)}\rangle$$

where \hat{W} is given by (3.15) and $\hat{\varepsilon}$ and \hat{p} are expressed in the j basis. The solutions for a given \mathcal{P} , expanded in the j basis, are

$$|\lambda^{(fw)}(\mathcal{P})\rangle = \sum_j |j\rangle \langle j | \exp\left(\frac{i\mathcal{P}}{2} \hat{z}\right) |\lambda\rangle = \sum_j I_{j\lambda}\left(\frac{\mathcal{P}}{2}\right) |j\rangle \quad (3.19)$$

where

$$|\lambda\rangle \equiv |\lambda^{(fw)}(0)\rangle.$$

Hence, the nature of the 'far-wall' limit states is determined by the behaviour of the

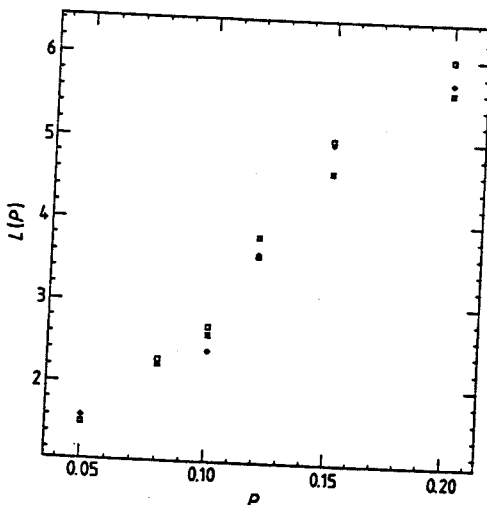


Figure 9. Average localisation length against \mathcal{P} , for $\mathcal{T}=100(\square)$, $500(\circ)$ and $1000(\diamond)$.

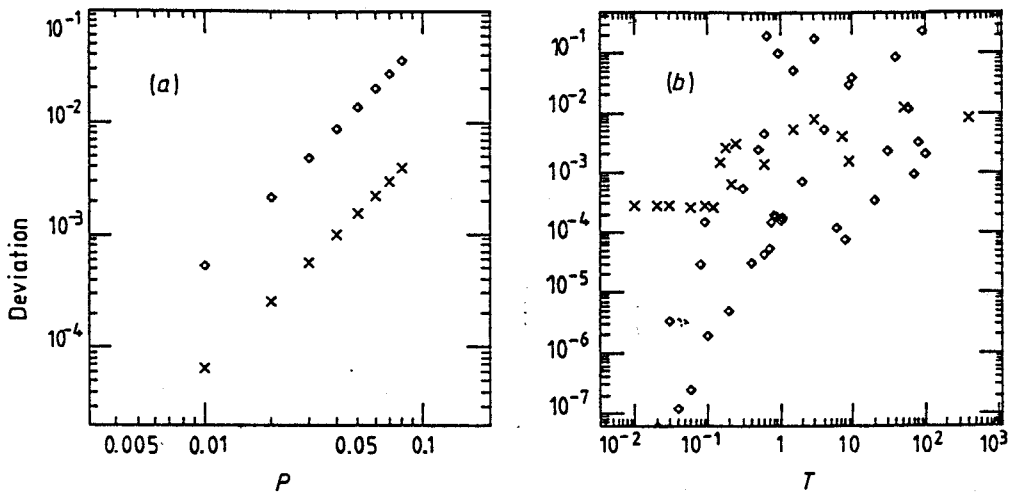


Figure 10. Deviation of the 'far-wall' QE eigenstates and spectrum (\times , $(\omega_\lambda - \omega_\lambda^{(fw)})/\omega_\lambda$; \diamond , $|1 - \langle \lambda | \lambda^{(fw)} \rangle|$); (a) deviation against \mathcal{P} , for $\mathcal{T} = 5.0$; (b) deviation against \mathcal{T} , for $\mathcal{P} = 0.08$.

$I_{jk}(\mathcal{P})$: they are localised over few near-diagonal j states, and decay as $\sim |j - \lambda|^{-4/3}$ for large $|j - \lambda|$.

To check the applicability of the 'far-wall' approximation in the ($\mathcal{T}/J^{1/3} \ll 2\pi$) domain, we calculated the overlap $\langle \lambda | \lambda^{(fw)} \rangle$ and the differences in the corresponding quasi-energies. In the domain where the 'far-wall' approximation is expected to be valid, it gives a very accurate description of the QE spectrum and eigenstates (figure 10).

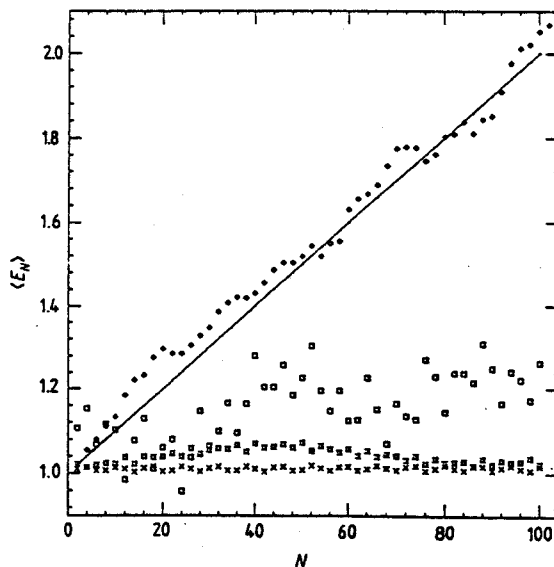


Figure 11. Comparison of the quantum and the classical (\diamond) dependence of the average energy on time; $P = 0.1$, $T = 100$. The quantum calculations were performed for $\hbar = 1/3$ (\square), $\hbar = 1$ (\triangle), $\hbar = 5$ (\times). The full line is the result of the simple random walk model (see equation (2.21)).

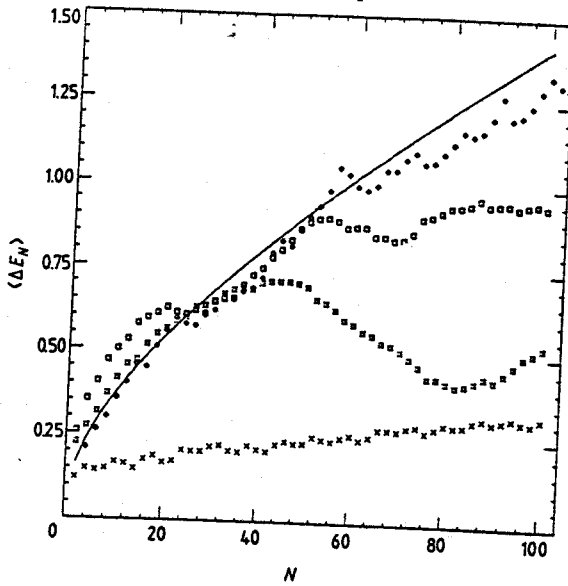


Figure 12. Comparison of the quantum and the classical dependence of the energy width on time; $P = 0.1$, $T = 100$. The quantum calculations were performed for the same values of \hbar as in figure 11. The full line is the result of the simple random walk model (equation (2.22)).

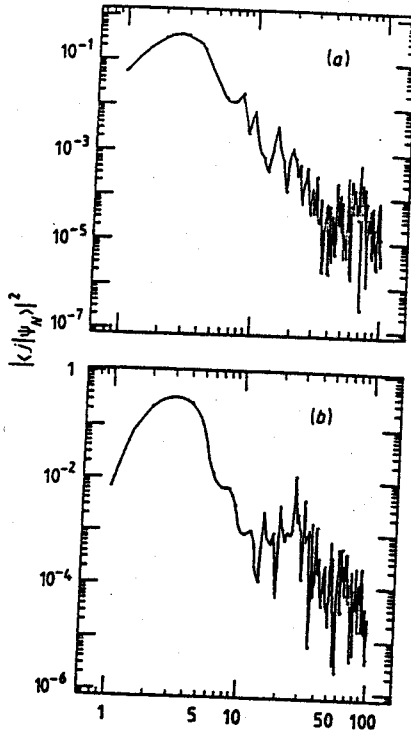


Figure 13. The projection of the wavefunction ψ_N on the 'bubble' eigenstates $|j\rangle$ after (a) $N = 20$ and (b) $N = 100$ periods of the external perturbation. Here, $\hbar = \frac{1}{3}$ ($\varphi = 0.25$, $\mathcal{T} = 250$).

The structure of the QE eigenstates has immediate consequences for the time evolution of the system. Of particular interest is the dependence of the moments of the energy distribution on the exposure time. The classical theory predicts that the first two moments increase linearly with N as long as the system is in the chaotic domain. In figures 11 and 12 we compare the quantum and the classical calculations. The quantum results are shown for a few values of \hbar . We see that the agreement between the classical and the quantum results is limited to the first stages of the exposure. Beyond a critical exposure time N^* , the classical diffusion is suppressed by quantum effects. N^* is a decreasing function of \hbar . The quantum suppression of classical diffusion is due to the initial exponential localisation of the QE eigenstates.

In figure 13 we show the distribution of the population probabilities $|\langle j | \psi_N \rangle|^2$ after $N = 20$ and $N = 100$ cycles of the external field. The high- j probabilities follow approximately a power-law fall-off, which is due to the corresponding asymptotic structure of the QE eigenstates. This in turn implies that the higher moments of the energy distribution (with orders $n \geq 3$) do not converge.

In the domain where the 'far-wall' approximation is valid, the quantum results are similar to the classical counterpart in predicting negligible growth of the mean energy and a suppressed diffusion. The QE states (figure 8(c) and (d)) do not show a unique exponential fall-off in any meaningful range of j values, and therefore the assignment of a localisation length becomes impossible. A simple relation between classical diffusion and quantum localisation cannot be applied for this domain.

4. Discussion and conclusions

In the present section we shall try to summarise our results in the light of the questions which were posed in the introductory remarks. The most prominent feature of the present system is that its unperturbed spectrum is unbounded but the differences between successive states (or in classical language its frequencies) decrease as the energy increases. This has the important consequence that the ratio between the driving frequency and the unperturbed orbital frequency varies with energy so that at high energies the motion becomes almost regular and an asymptotic (classical as well as quantal) constant of the motion emerges. In this respect the 'bubble' system resembles the RF-driven hydrogen atom with the exception that its unperturbed spectrum is not complicated by a continuum component. In the kicked rotor the classical frequencies increase linearly with energy and since the $\delta(t)$ impulses have equal amplitudes for all the harmonics of the basic period, it is always possible to match the rotation frequency with one of the harmonics of the driving frequency. Therefore, all the properties which characterise the dynamics of the kicked rotor *globally*, will at most appear *locally* in the 'bubble' and the driven hydrogen systems. This feature indeed marks the classical as well as the quantal description of the latter systems.

In the classically chaotic regime the 'bubble' quasi-energy states are localised exponentially in the vicinity of the localisation centres. Two ingredients are necessary to induce Anderson-like localisation: the factors $\exp(i\mathcal{J}j^{2/3})$ (see equation (3.12)) should introduce pseudorandom phases to the evolution operator, and the evolution operator should couple states only within a finite range. In the 'bubble' system the first requirement is met only for high- \mathcal{J} and low- j values, for which $\mathcal{J}j^{-1/3} > 2\pi$. Even in this domain it is not certain that the phases are sufficiently

uncorrelated to induce proper exponential localisation [24]. The second requirement is not strictly met either. The integrals $I_{jk}(\mathcal{P})$ decrease only as $|j-k|^{-4/3}$ and hence it is hard to assign a finite range to the evolution operator. (This should be contrasted with the kicked rotor case where beyond a certain range the matrix elements of the evolution operator decrease faster than exponentially!) Our numerical results seem to suggest that in spite of the fact that the conditions to induce exponential localisation are met only marginally, localisation does occur whenever the corresponding classical dynamics is fully chaotic. However, the localisation length is not proportional to the classical diffusion constant. The proportionality between these two quantities is expected from general arguments of localisation theory [25]. The fact that our results do not agree with these expectations is probably due to the 'bubble' failure to meet the requirements stated above. Currently we are not able to isolate the specific feature which is to blame for the non-standard behaviour of the 'bubble' system. Our results show, however, that the quantum limit of classical diffusion induced by chaos may be richer and not necessarily exhausted by the results derived from the study of the kicked rotor.

Since the 'bubble' model was formerly introduced as a simplification of an experimental system (§1), we add a few remarks on the experimental realisation of this system. We can estimate the order of magnitude for the various quantities involved in the physical system, in which one may measure the effects discussed in this work. Consider the experimental set-up of Poitrenaud and Williams [16], in which the effective mass of both the positively and negatively charged 'bubbles' was measured. We assume the mass of each type of 'bubble' to be known, and calculate the uniform electric field F corresponding to various excitation energies. Denoting by α_+ and α_- the scaling parameters which correspond, respectively, to the masses of the positive and negative ions, and by F the electric field in V cm^{-1} , one obtains

$$\alpha_+ = 6.3 \times 10^{18} F^{-2/3} \text{ erg}^{-1} \quad \alpha_- = 1.1 \times 10^{19} F^{-2/3} \text{ erg}^{-1}. \quad (4.1)$$

Using (4.1), one can compute the required F for which a reasonable excitation energy of 0.5 K corresponds to the quantum numbers $j=1$, $j=10$ and $j=100$: denote the appropriate fields by F_1 , F_{10} and F_{100} , respectively; then for the positively charged 'bubbles'

$$F_1 = 1800 \text{ V cm}^{-1} \quad F_{10} = 200 \text{ V cm}^{-1} \quad F_{100} = 20 \text{ V cm}^{-1}.$$

For the negatively charged 'bubbles', the field should be approximately twice as strong for the same excitation energies (and of the opposite sign). For high j , $F_j \propto 1/j$.

The above calculations show that one can measure a wide range of energy levels in the laboratory. It is still left to estimate the parameters of the driving force, which were simulated by means of the frequency $1/2\mathcal{T}$ and the momentum transfer \mathcal{P} . Inserting α_+ or α_- into the inversion of (3.2), for a typical electric field of $\sim 100 \text{ V cm}^{-1}$, one obtains the following: for \mathcal{T} values in the range 0.1–100, the appropriate physical frequencies are in the range 100 MHz to 100 GHz—i.e. in the microwave scale. The sinusoidal electric field associated with the driving force F_{dr} is related to the constant field F via $F_{\text{dr}} = \mathcal{P}F/\mathcal{T}$.

Acknowledgements

We are grateful to Professor W F Vinen for bringing to our attention the 'bubble' system and pointing out its relevance to quantum chaos. We would also like to thank

Drs R Blümel and S Fishman for numerous discussions and helpful suggestions. This research was supported in part by the Israeli Basic Research Commission.

Appendix

The matrix elements of the kick propagator in the position representation, for any j and k , are defined as

$$I_{jk}(\mathcal{P}) = \int_0^{\infty} \bar{\psi}_j(z) \bar{\psi}_k(z) \exp(i\mathcal{P}z) dz \quad \text{where} \quad \bar{\psi}_j \equiv \frac{\text{Ai}(z - \varepsilon_j)}{\text{Ai}'(-\varepsilon_j)}. \quad (\text{A1})$$

The integrals (A1) have no simple analytic solution, basically because of the singular nature of this problem—i.e. since they are performed over half the space only. Alternatively, we use a calculation method which is rather complicated, but gives the desired results up to any specified accuracy.

$I_{jk}(\mathcal{P})$ is a complex function of the real parameter \mathcal{P} ; we try to expand it in the form

$$I_{jk}(\mathcal{P}) = \sum_{n=1}^{\infty} g_n(j, k) \mathcal{P}^n \quad \text{where} \quad g_n(j, k) \equiv \frac{I_{jk}^{(n)}(0)}{n!}. \quad (\text{A2})$$

Using the special properties of Airy's function, we derive below a recursion relation, from which $g_n(j, k)$ can be calculated in terms of the lower derivatives.

We calculate the first derivative of $I_{jk}(\mathcal{P})$ with respect to \mathcal{P} :

$$-i \frac{dI_{jk}(\mathcal{P})}{d\mathcal{P}} = \int_0^{\infty} z \bar{\psi}_j(z) \bar{\psi}_k(z) \exp(i\mathcal{P}z) dz \quad (\text{A3})$$

and define a new function $h(z)$ so that

$$\frac{dh(z)}{dz} \equiv z \bar{\psi}_j(z) \bar{\psi}_k(z).$$

Then

$$h(z) = \frac{(h_1(z) + h_2(z) + h_3(z))}{(\varepsilon_j - \varepsilon_k)^2}$$

where

$$\begin{aligned} h_1(z) &\equiv (\varepsilon_j + \varepsilon_k - 2z) \bar{\psi}_j(z) \bar{\psi}_k(z) \\ h_2(z) &\equiv \frac{(\varepsilon_j - \varepsilon_k)^2 z + 2}{(\varepsilon_j - \varepsilon_k)} (\bar{\psi}_j(z) \bar{\psi}_k'(z) - \bar{\psi}_j'(z) \bar{\psi}_k(z)) \\ h_3(z) &= 2 \bar{\psi}_j'(z) \bar{\psi}_k'(z). \end{aligned} \quad (\text{A4})$$

Equation (A4) was derived in [22]. The primes denote derivatives with respect to z . Using integration by parts, (A3) in terms of $h(z)$ becomes

$$-i \frac{dI_{jk}(\mathcal{P})}{d\mathcal{P}} = h(z) \exp(i\mathcal{P}z) \Big|_0^{\infty} - i\mathcal{P} \int_0^{\infty} h(z) \exp(i\mathcal{P}z) dz. \quad (\text{A5})$$

The first term in (A5), with the help of the boundary conditions on $\bar{\psi}_j(z)$ and $\bar{\psi}_k(z)$

reduces to

$$\frac{-2\bar{\psi}'_j(0)\bar{\psi}'_k(0)}{(\varepsilon_j - \varepsilon_k)^2} = \frac{-2}{(\varepsilon_j - \varepsilon_k)^2}.$$

To calculate the second term, $h(z)$ in the integrand was separated into the three functions defined in (A4); each integral is calculated separately:

$$\int_0^\infty h_1(z)\exp(i\mathcal{P}z) dz = (\varepsilon_j + \varepsilon_k)I_{jk}(\mathcal{P}) + 2i \frac{dI_{jk}(\mathcal{P})}{d\mathcal{P}}. \quad (\text{A6})$$

Using the properties of Airy's function,

$$\begin{aligned} & [\text{Ai}'(z - \varepsilon_j)\text{Ai}(z - \varepsilon_k) - \text{Ai}(z - \varepsilon_j)\text{Ai}'(z - \varepsilon_k)]' \\ &= \text{Ai}''(z - \varepsilon_j)\text{Ai}(z - \varepsilon_k) - \text{Ai}(z - \varepsilon_j)\text{Ai}''(z - \varepsilon_k) \\ &= -(\varepsilon_j - \varepsilon_k)\text{Ai}(z - \varepsilon_j)\text{Ai}(z - \varepsilon_k) \end{aligned} \quad (\text{A7})$$

one obtains for the second integral

$$\begin{aligned} \int_0^\infty h_2(z)\exp(i\mathcal{P}z) dz &= \frac{h_2(z)}{i\mathcal{P}} \exp(i\mathcal{P}z) \Big|_0^\infty - \frac{1}{i\mathcal{P}} \int_0^\infty \exp(i\mathcal{P}z)h_2'(z) dz \\ &= -\left(\frac{(\varepsilon_j - \varepsilon_k)^2}{\mathcal{P}^2} + \frac{2}{i\mathcal{P}}\right)I_{jk}(\mathcal{P}) + \frac{(\varepsilon_j - \varepsilon_k)^2}{\mathcal{P}} \frac{dI_{jk}(\mathcal{P})}{d\mathcal{P}}. \end{aligned} \quad (\text{A8})$$

The function $h_3(z)$ can be rewritten by means of the identity

$$2\text{Ai}'(z - \varepsilon_j)\text{Ai}'(z - \varepsilon_k) = [\text{Ai}(z - \varepsilon_j)\text{Ai}(z - \varepsilon_k)]'' + [(\varepsilon_j + \varepsilon_k) - 2z]\text{Ai}(z - \varepsilon_j)\text{Ai}(z - \varepsilon_k). \quad (\text{A9})$$

Thus, the third integral is evaluated using a double integration by parts, the boundary conditions and (A6):

$$\int_0^\infty h_3(z)\exp(i\mathcal{P}z) dz = [(\varepsilon_j + \varepsilon_k) - \mathcal{P}^2]I_{jk}(\mathcal{P}) + 2i \frac{dI_{jk}(\mathcal{P})}{d\mathcal{P}}. \quad (\text{A10})$$

Inserting equations (A6), (A8) and (A10) into (A5), multiplied by $(\varepsilon_j - \varepsilon_k)^2/(-i\mathcal{P})$, one obtains the differential equation

$$\frac{dI_{jk}(\mathcal{P})}{d\mathcal{P}} + \frac{i}{2} \left(\frac{(\varepsilon_j - \varepsilon_k)^2}{2\mathcal{P}^2} - \frac{i}{\mathcal{P}} + \frac{\mathcal{P}^2}{2} - (\varepsilon_j + \varepsilon_k) \right) I_{jk}(\mathcal{P}) = \frac{1}{2\mathcal{P}}. \quad (\text{A11})$$

Equation (A11) can be further differentiated. In the diagonal case, for $\mathcal{P} = 0$ one obtains a recursion relation for the higher derivatives:

$$I_{jj}^{(n)} \left(2 \binom{n}{1} + \binom{n}{0} \right) - I_{jj}^{(n-1)} 2i\varepsilon_j \binom{n}{1} + I_{jj}^{(n-3)} \binom{n}{3} = 0 \quad \forall n \geq 3. \quad (\text{A12})$$

In terms of the coefficients $g_n(j, j)$, defined by (A2), one obtains the recursion relation

$$(2n + 1)g_n(j, j) - 2i\varepsilon_j g_{n-1}(j, j) + \frac{i}{2} g_{n-3}(j, j) = 0. \quad (\text{A13})$$

for each $n \geq 3$. The complete solution for the $g_n(j, j)$ is determined from (A13),

together with the independent evaluation of the first derivatives at $\mathcal{P} = 0$:

$$g_0(j, j) = I_{jj}(0) = 1 \quad g_1(j, j) = \frac{2i}{3} \varepsilon_j \quad g_2(j, j) = -\frac{4}{15} \varepsilon_j^2 \quad (\text{A14})$$

The coefficients $g_1(j, j)$ and $g_2(j, j)$ are explicitly calculated with the help of [22] and the boundary conditions; $g_0(j, j)$ is just the normalisation condition. The resulting series ((A2) for $k = j$) is converging if $\mathcal{P} < 1$, since (recall (A13)) the coefficients satisfy

$$\frac{g_{n-1}(j, j)}{g_n(j, j)} \sim \frac{1}{n}$$

thus

$$\left| \frac{g_{n-1}(j, j)}{g_n(j, j)} \right| < 1$$

hence it can be approximated by the truncated sum, up to any desired accuracy:

$$I_{jj}^N(\mathcal{P}) = \sum_{n=1}^N g_n(j, j) \mathcal{P}^n \quad (\text{A15})$$

N is determined according to \mathcal{P} and the required accuracy.

In the off-diagonal case ($j \neq k$), the recursion relation for $g_n(j, k)$ for $n \geq 4$, can be derived by inserting the power expansion $I_{jk}(\mathcal{P}) = \sum_n g_n(j, k) \mathcal{P}^n$ into (A11), and equating the coefficients. The result is

$$g_n(j, k) = \left((n - \frac{1}{2})g_{n-1}(j, k) - \frac{i}{2}(\varepsilon_j + \varepsilon_k)g_{n-2}(j, k) + \frac{i}{4}g_{n-4}(j, k) \right) \frac{4i}{(\varepsilon_j - \varepsilon_k)^2} \quad (\text{A16})$$

(A16) is used together with the set of equations

$$g_0(i, k) = 0 \quad g_1(j, k) = \frac{-2i}{(\varepsilon_j - \varepsilon_k)^2} \quad g_2(j, k) = \frac{12}{(\varepsilon_j - \varepsilon_k)^4} \\ g_3(j, k) = \frac{4i}{(\varepsilon_j - \varepsilon_k)^6} [30 - (\varepsilon_j - \varepsilon_k)^2(\varepsilon_j + \varepsilon_k)]. \quad (\text{A17})$$

Equation (A17) is derived similarly to equation (A14), by determining the first derivatives of $I_{jk}(\mathcal{P})$ at $\mathcal{P} = 0$ for $j \neq k$, and adding the orthogonality condition. However, the resulting series is asymptotic: the coefficients diverge above some n ; therefore, the accuracy of this method is limited, unless \mathcal{P} is very small. The method becomes practically useless for the large- j near-diagonals. This is due to the fact that for large n the $g_n(j, k)$ diverge as

$$\frac{1}{(\varepsilon_j - \varepsilon_k)^{2n}} \sim (j^{2/3})^n.$$

Hence, we have to use an alternative computation method for $j \sim k$.

Assume that for some small \mathcal{P}_0 , the previous method is accurate enough to calculate $I_{jk}(\mathcal{P}_0)$. Then one can solve for $I_{jk}(\mathcal{P})$ by straightforward integration of (A11):

$$I_{jk}(\mathcal{P}) = \int_{\mathcal{P}_0}^{\mathcal{P}} \exp\left(-\int_p^{\mathcal{P}} F_{jk}(p') dp'\right) G(p) dp + I_{jk}(\mathcal{P}_0) \exp\left(-\int_{\mathcal{P}_0}^{\mathcal{P}} F(p) dp\right)$$

where

$$F_{jk}(\mathcal{P}) \equiv \frac{i}{2} \left(\frac{(\varepsilon_j - \varepsilon_k)^2}{2\mathcal{P}^2} - \frac{i}{\mathcal{P}} + \frac{\mathcal{P}^2}{2} - (\varepsilon_j + \varepsilon_k) \right) \quad G(\mathcal{P}) = \frac{1}{2\mathcal{P}}. \quad (\text{A18})$$

The integrals in (A18) can be performed numerically, and since the integration is to be used only when $(\varepsilon_j - \varepsilon_k)$ is small, the numerical integration of (A18) does not pose any problem.

The truncation of the basis size gives rise to a serious problem: the truncated propagator is not unitary. The deviation from unitarity is not large, but is enough to cause a remarkable decay of the normalisation of the time-dependent state $|\psi_N\rangle$, if N is large. In order to remove this artefact, we construct a unitary matrix out of $I_{jk}(\mathcal{P})$, without changing it significantly. First, we diagonalise the real part of $I_{jk}(\mathcal{P})$, which would correspond to $\langle j | \cos(\mathcal{P}\hat{z}) | k \rangle$ if $I_{jk}(\mathcal{P})$ were truly unitary. Then, we define the 'unitarised' matrix as

$$I_{jk}^{\text{un}}(\mathcal{P}) \equiv \sum_{\beta} \langle j | \beta \rangle \exp(i \cos^{-1}(\beta)) \langle \beta | k \rangle \quad (\text{A19})$$

where the β are the eigenvalues of the real matrix and $|\beta\rangle$ are the corresponding eigenvectors. Whenever unitarity is important, we use $I_{jk}^{\text{un}}(\mathcal{P})$ in the calculations instead of $I_{jk}(\mathcal{P})$.

References

- [1] Casati G, Chirikov B V, Izrailev F M and Ford J 1979 *Stochastic Behavior in Classical and Quantum Hamiltonian Systems, Springer Lecture Notes in Physics* vol 93 ed G Casati and J Ford (Berlin: Springer)
- [2] Fishman S, Grepel D R and Prange R E 1982 *Phys. Rev. Lett.* **49** 509
Grepel D R, Prange R E and Fishman S 1984 *Phys. Rev. A* **29** 1639
- [3] Hogg T and Huberman B A 1982 *Phys. Rev. Lett.* **48** 711; 1983 *Phys. Rev. A* **28** 22
- [4] Blümel R, Fishman S and Smilansky U 1986 *J. Chem. Phys.* **84** 5
- [5] Shepelyansky D L 1986 *Phys. Rev. Lett.* **56** 677
- [6] Bayfield J E and Koch P M 1974 *Phys. Rev. Lett.* **33** 258
Bayfield J E, Gardner L D and Koch P M 1977 *Phys. Rev. Lett.* **39** 76
- [7] Koch P M 1986 *Proc. NATO Advanced Research Workshop on Fundamental Aspects of Quantum Theory, Como, Italy (1985)* ed V Gorini and A Frigerio (London: Plenum)
- [8] Koch P M 1987 *Proc. 1st Int. Conf. on the Physics of the Phase Space, University of Maryland, 20-23 May, 1986 (Physics of the Phase Space, Springer Lecture Notes in Physics (Berlin: Springer) to be published)*
- [9] Leopold J G and Percival I C 1979 *J. Phys. B: At. Mol. Phys.* **12** 709
- [10] Casati G, Chirikov B V, Shepelyansky D L and Guarneri I 1986 *Phys. Rev. Lett.* **57** 823; 1987 *Phys. Rep.* **154** 77
Casati G, Chirikov B V, Guarneri I and Shepelyansky D L 1986 *Phys. Rev. Lett.* **56** 2437
- [11] Leopold J G and Richards D 1986 *J. Phys. B: At. Mol. Phys.* **19** 1125
Rath O and Richards D in preparation
- [12] Jensen R V 1984 *Phys. Rev. A* **30** 386
Leopold J G and Richards D 1985 *J. Phys. B: At. Mol. Phys.* **18** 3369
- [13] Blümel R and Smilansky U 1984 *Phys. Rev. A* **30** 1040; 1987 *Rev. Lett.* **58** 2531
- [14] Delone N B, Krainov B P and Shepelyansky D L 1983 *Usp. Fiz. Nauk.* **140** 355 (*Sov. Phys.-Usp.* **26** 551)
- [15] Blümel R and Smilansky U 1987 *Z. Phys. D* **6** 83
Bardsley J N, Sundaram B, Pinnaduwaage L A and Bayfield J E 1986 *Phys. Rev. Lett.* **56** 1007
- [16] Poitrenaud J and Williams F I B 1972 *Phys. Rev. Lett.* **29** 1230
- [17] Fetter A L 1976 *The Physics of Liquid and Solid Helium* ed K H Bennemann and J B Ketterson (New York: Wiley) part 1, ch 3, p 207

- [18] Chirikov B V 1979 *Phys. Rep.* **52** 263
- [19] Abramowitz M and Stegun I A 1964 *Handbook of Mathematical Functions* (New York: Dover)
- [20] Berry M V, Balazs N L, Tabor M and Voros A 1979 *Ann. Phys.* **122** 26
Zaslavsky G M 1981 *Phys. Rep.* **80** 158
- [21] Zeldovich Ya B 1967 *Sov. Phys.-JETP* **24** 1006
Chu S 1981 *J. Chem. Phys.* **75** 2215
Dion D R and Hirschfelder J O 1976 *Adv. Chem. Phys.* **35** 265
Gesztelyi F and Mitter H 1981 *J. Phys. A: Math. Gen.* **14** L79
- [22] Gordon R 1969 *J. Chem. Phys.* **51** 14 Appendix A
- [23] Englman R and Levi P 1963 *J. Math. Phys.* **4** 105
- [24] Griniasti M and Fishman S 1986 private communication
- [25] Fishman S 1986 *Proc. Int. Conf. on Chaos and Related Nonlinear Phenomena; Where Do We Go from Here? Kyriat Anavim, 1986* ed I Procaccia (New York: Plenum) in press